A Direct Mapping Approach to Understand Carrier Relaxation Dynamics in Varied Regions of a Polycrystalline Perovskite Film

Amir Fathi,[a] Efat Jokar,[b] Yuan-Pern Lee,[a],[b] and Eric Wei-Guang Diau*,[a],[b]

ABSTRACT: We developed a direct mapping approach to overlay the image of a polycrystalline perovskite film obtained from the transient absorption microscope (TAM) with that from the scanning electron microscope (SEM). By mapping these imaging data pixel by pixel, we are able to observe the relaxation dynamics of the photogenerated charge carriers on varied regions of the film. The carrier relaxation dynamics contain a dominated single-exponential decay component due to the recombination of charge carriers. We found that the lifetime distribution of charge recombination shows a bimodal feature, for which the rapid and slow distributions are assigned as free and trapped carriers, respectively. The charge recombination was slower in the grain boundary (GB) region than in the grain interior (GI) region. The small grains have longer lifetimes than the large grains for the crystal size smaller than 500 nm. Our results thus indicate that GB with retarded charge recombination might play a positive role in a perovskite solar cell.

Organo-inorganic halide perovskites have attracted much attentions due to their successful applications not only for photovoltaics,[1–3] but also for other potential optoelectronic applications.[4–6] However, fundamental understanding of the operational mechanism for a perovskite solar cell (PSC) has not been well recognized. In principle, the performance of a PSC is proportional to how far the photogenerated charge carriers can travel so that they can be effectively collected at the terminals. The limiting factors for rapid charge separation and slow charge recombination are determined by how many trap states, defects and dislocations of the carriers throughout the perovskite film in bulk crystals or in the boundaries of the crystals.[7] There have been reported that the bigger size of the crystals gives the better overall device performance due to a better crystal growth control to increase the charge transport rate and to decrease the electron-hole recombination rate.[7–12] In contrast, Don et al.[13] reported that the size-dependent factor reaches a counter-intuitive point where larger crystal grains may cause more voids to give a negative effect on device performance. Moreover, the positive roles of grain boundaries (GB) on charge recombination and device performance have been reported experimentally[14–16] and theoretically.[17] These controversial conclusions indicate the necessity of real-time probing of the charge carrier relaxation dynamics on varied regions of the perovskite film using ultrafast imaging techniques reported elsewhere.[18,19] Although some time-resolved optical microscopy (OM) techniques have been reported to show carrier relaxation dynamics[20,21] and effect of hot carrier cooling in $MAPbI_3$ perovskite films,[22–24] the observed OM lifetime images are difficult to directly correlate with those obtained from a scanning electron microscope (SEM) due to the poor spatial resolution of the former resulting from the optical diffraction limit. To solve this problem, in the present study we developed a novel mapping technique to match the image of a femtosecond (fs) transient absorption microscopy (TAM) with the SEM image for which both images were obtained from the same perovskite film. Based on this approach, the carrier relaxation dynamics can be measured pixel-by-pixel and the corresponding lifetime distributions were analyzed accordingly for the charge recombination in varied locations of the perovskite film.

The $MAPbI_3$ perovskite film was prepared via a solution-processing procedure reported elsewhere;[25] the crystal morphology (SEM) and its corresponding optical properties (absorption and PL) are shown in Figures S1a and S1b, Supporting Information (SI), respectively. The sample was sandwiched and sealed with a microscope coverslip and mounted upside down with the sealing coverslip facing the objective. The experimental setup for the fs TAM measurements is shown in Figure S2, SI. The pump is selected at 600 nm and the probe is set at the band-edge of the sample (770 nm). The pump and probe fluences were ~1 and ~3 $\mu J\ cm^{-2}$, respectively, for which the pump fluence was low enough to avoid any other higher order charge recombination reported elsewhere.[26,27] The TAM image was first taken on a small field of view (FOV) with the size 6.6 x 6.6 μm^2 (256 pixels by 256 pixels) and the range of the time delays between pump and probe pulses extended up to 1200 ps. After the TAM imaging scan was finished, the sample was etched with a high laser power (~10 mW). Two kinds of markers were done: first, the film was etched with a spot at the left-bottom corner of the FOV; second, the film was etched with two large co-centered squares (33 x 33 and 44 x 44 μm^2) outside the FOV. The TAM intensity image at the maximum signal (time zero) was then taken again followed by taking the SEM image on the same etched sample. The co-centered square markers on the sample can be found in SEM by panning the FOV slowly and the spot marker is needed to determine the orientation of the film. The matching images of both TAM and SEM are visualized in Figure S3, SI.

To precisely match the TAM and SEM images within the small FOV taken before etching, there are a few steps necessary to be done. First, we consider a larger size of the SEM image including the spot-etched area (Figure 1a) so that the TEM image can be

[a] A. Fathi, Dr. Y.-P. Lee, Dr. E. W.-G. Diau Department of Applied Chemistry and Institute of Molecular Science, National Chiao Tung University
1001 Ta-Hsueh Rd., Hsinchu 30010, Taiwan
E-mail: diau@mail.nctu.edu.tw
[b] Dr. E. Jokar, Dr. Y.-P. Lee, Dr. E. W.-G. Diau
Center for Emergent Functional Matter Science, National Chiao Tung University
1001 Ta-Hsueh Rd., Hsinchu 30010, Taiwan

Supporting information for this article is given via a link at the end of the document.

done in the same area with good spatial resolution to match with the TEM image. Second, we convoluted this etched SEM image with a simulated point spread function (PSF) to generate a simulated TAM image (Sim-TAM, Figure 1b) with the coordinates for the SEM image. This step is needed because the etched SEM image itself does not have clear correlations with the etched TAM image (Figure 1c). Third, we can now match the coordinates of the TAM image with those of the Sim-TAM image (Figure 1d) in the original FOV (6.6 x 6.6 μm^2). Finally, the matching coordinates were used to overlay the TAM image on top of the SEM image, as shown in Figure 1e. The successful image mapping between the TAM intensity at time zero and the SEM morphology can be visualized in a small window with the size of FOV 4.4 x 4.4 μm^2, as shown in Figure 1f. To confirm that the marking process did not cause any photo-degradation, the TAM images before and after etching were taken and compared in Figure S4, SI. The SEM image with a larger FOV (Figure S5, SI) does not show any photo-damage outside the laser ablation region.

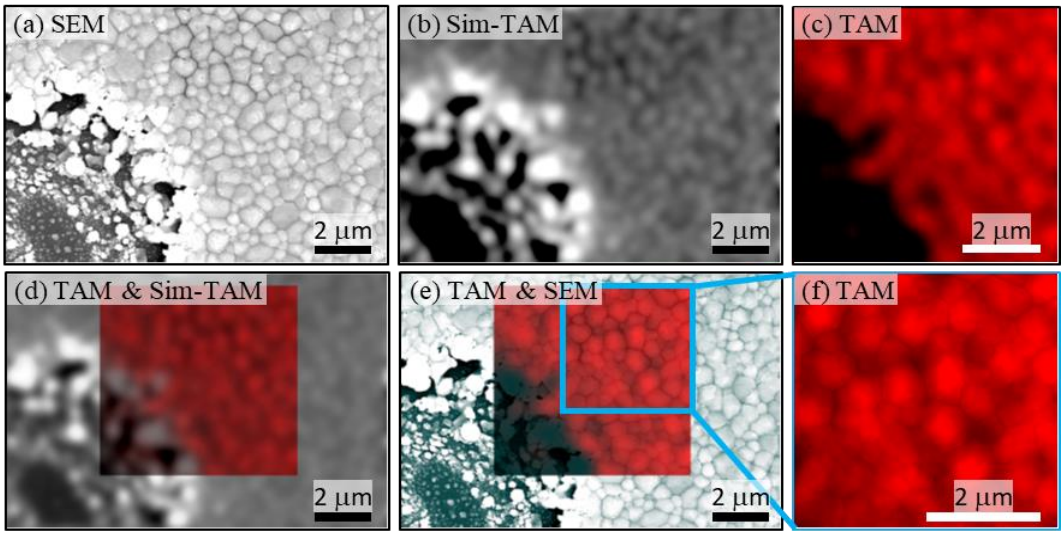

Figure 1. Steps towards finding the precise matching between SEM and TAM images of a polycrystalline $MAPbI_3$ film: (a) SEM image with the spot etching pattern to be matched with the TAM intensity image; (b) simulated TAM image (Sim-TAM) by convolution of the SEM image with the simulated point spread function (PSF); (c) the TAM intensity image obtained at time zero; (d) mapping of the TAM image with the Sim-TAM image to produce the matching coordinates for SEM; (e) the TAM intensity image mapped on top of the SEM image; (f) the matched TAM/SEM images in a small field of view (FOV).

The TAM intensity image shown in Figure 1f indicates that, upon excitation at 600 nm, the crystals generated more charge carriers in the grain interiors (GI) than in their GB. The grains with high intensity might reflect those crystal grains with great crystallinity. In contrast, the grains with low intensity might imply their poor crystallinity with certain defects or trap states in the crystal. For clarity, the TA intensities are normalized to 0 – 1 and segmented into three regions, low (0-0.3), mid (0.3-0.7) and high (0.7-1) intensities. The corresponding TAM/SEM mapping images and the color-corded histograms of intensities are shown respectively in Figures S6a and b, SI. As shown in Figure 2, the blue-coded pixels (low intensity, Figure 2a) are mostly accumulated around the GB region whereas the red-coded pixels (high intensity, Figure 2c) are mostly accumulated in the GI region; the green-coded pixels (mid intensity, Figure 2b) are evenly distributed all over the film. The corresponding decay kinetics would be analyzed pixel-by-pixel for the TAM image in varied regions of the film.

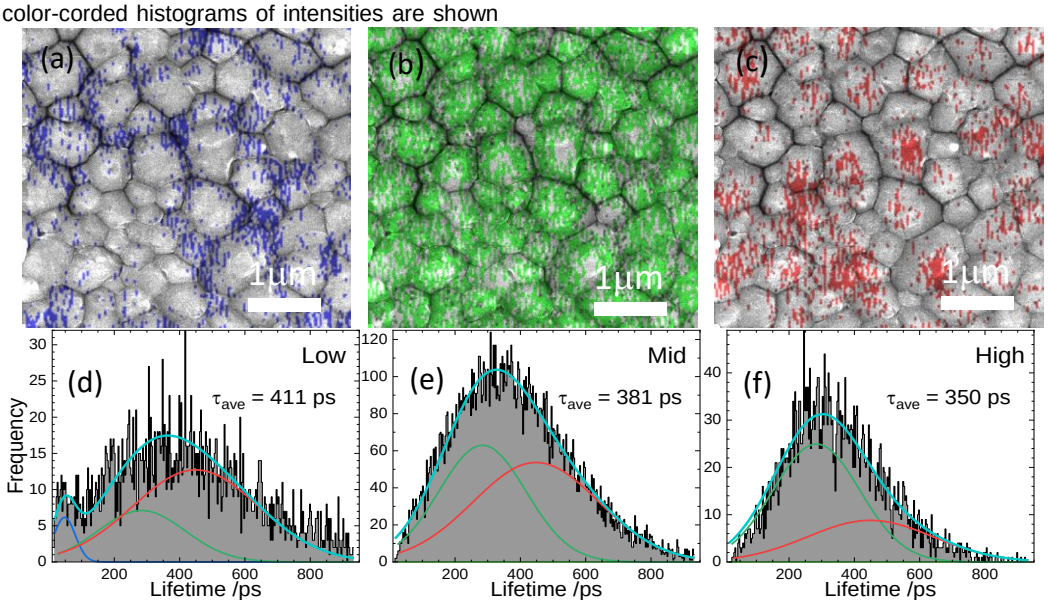

Figure 2. TAM intensity images (a-c) and the corresponding histograms of the lifetime distributions (d-f) for the normalized TA intensities in the three scales (a/d) low intensity: 0-0.3, (b/e) mid intensity: 0.3-0.7 and (c/f) high intensity: 0.7-1.

For the carrier relaxation dynamics in each pixel, the TA decay profiles can be fitted by convolution of the instrument response function (IRF ~0.5 ps) with the kinetics involving three components – a Gaussian function representing the thermal lensing effect,[28] a single exponential decay function representing the recombination of charge carriers and an offset signal representing the long-lived carriers. The above kinetic model is described in equation S1, SI. We discovered that the carrier relaxation lifetimes are broadly distributed in varied crystal regions of the film; the histogram of the lifetime distribution of the whole FOV is shown in Figure S7, SI. It is noted that the observed carrier relaxation lifetimes are highly correlated to the quality of the film in different areas with a broad lifetime distribution in the range 16 – 933 ps; the average (mean) lifetime (τ_{ave}) of the distribution is 380 ps. Since this lifetime distribution shows an asymmetrical feature, it was fitted by two Gaussian functions with the peak positions at 281 and 447 ps, respectively. This bimodal lifetime distribution feature (sample 1) has been confirmed by another perovskite film (sample 2) fabricated with the same procedure but at a different day. The lifetime distribution of sample 2 was fitted with two Gaussians centered at 213 and 551 ps, respectively, with a mean lifetime 448 ps. Note that the long lifetime distribution of sample 2 is so pronounced and narrow whereas the short one is broadly distributed to extend to 1500 ps (Figure S8, SI; the corresponding color-coded intensity image is shown in Figure 9a, SI). Even though the two samples show different lifetime distributions, both demonstrate a bimodal lifetime distribution, which is a characteristic feature for a solution processed polycrystalline perovskite film that requires many well-controlled experimental steps to produce.

As shown in Figures 2d-f (sample 1) and Figures S9b-d, SI (sample 2), the relative amplitudes of the long and short lifetime distributions strongly depend on the normalized TA intensities. The intensity-dependent lifetime distributions of both samples show the contrast relative amplitude changes for the long and short lifetime distributions, for which the long/short amplitude ratios show a systematic trend for low intensity > mid intensity > high intensity. For sample 1, the mean lifetimes are 411, 381 and 350 ps for low, mid and high intensities, respectively; for sample 2, they are 538, 454 and 362 ps, respectively. Since the low-intensity and high-intensity pixels are most located at the GB and the GI regions (Figure S6a for sample 1 and Figure S9a for sample 2), respectively, our results thus indicate that the charge recombination is slower in the GB region with low TA intensities than in the GI region with high TA intensities. There is also an additional distribution with ultra-short lifetimes (< 100 ps) in the histogram of low intensity (Figure 2d) representing the structural defects in some low-intensity areas.

To understand the effect of mean lifetime on grain size, we calculated the mean lifetimes for each grain on both samples. Figures 3a and b show the SEM images for sample 1 and sample 2, respectively, with the boundaries of each crystal grain highlighted in yellow. In this way, the lifetime distributions of each grain can be determined and the corresponding mean lifetimes were plotted as a function of grain size for the two samples, as shown in Figure 3c. The total number of grains is 58 for sample 1 and 283 for sample 2. It is apparent that sample 1 contains more large grains than sample 2 with the average grain size (determined by the square root of the crystal area) in the range 150-900 nm, whereas sample 2 contains many small grains with the grain size in the range 100-700 nm. As shown in Figure 3c, the mean lifetimes of both samples match quite well for grain size larger than 500 nm with a constant lifetime ~380 ps. In contrast, for the grain size smaller than 500 nm, there is a clear increasing trend on mean lifetimes with decreasing the grain sizes. Note that the small grains also show large fluctuations on lifetimes because less pixels are averaged in small grains. Although the lifetimes of sample 1 still overlap with those of sample 2 within the uncertainties, the large contributions of long lifetimes on the small grains of sample 2 make the size-dependent effect on mean lifetimes more evident for sample 2 than for sample 1 (Figure 3c). Therefore, our results seem to show that the mean lifetimes are greater for the small grains than for the large grains when the crystals are smaller than 500 nm, and the lifetimes are independent on the grain size when the crystals are larger than 500 nm. This phenomenon is consistent with the fact that the small grains contain larger portions of GB with longer lifetimes than for the large grains, for which the latter is dominated by the contribution of GI that shows the constant lifetime for both samples.

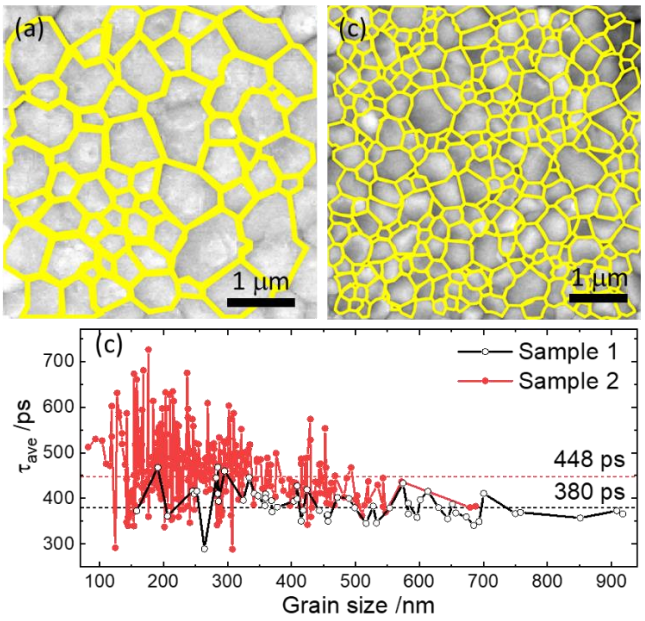

Figure 3. SEM images of (a) sample 1 and (b) sample 2 with the crystal grains highlighted in yellow; (c) the corresponding plots of mean lifetime (τ_{ave}) as a function of grain size for sample 1 (open circle) and sample 2 (solid circle). The mean lifetimes of the whole FOV of both samples are indicated.

Our direct-mapping results show that the charge recombination times are longer for the small grains with more contributions from the GB than for the large grains with more contributions from the GI. This observation has resolved the controversial issue for the influence of GB of a perovskite film on charge carrier recombination to play a positive role, in consistent with previous experimental results[14,16] and theoretical predictions.[17] According to theory, symmetry breaking at the GB creates trap states that leads to slower charge recombination in GB than in GI.[17] Therefore, we may assign the long and short lifetime distributions being due to the trapped and free charge carries undergoing charge recombination, respectively. For sample 2, the two lifetime distributions are well separated and the deep trapped charge carriers can be visualized in the SEM/TAM lifetime images (Figure S10, SI) showing the red pixels (τ_{ave} > 950 ps) distributed around the GB region and some small grains. In the study of Jiang et al.,[24] they concluded that the grain boundaries act as energy acceptors to accelerate hot carrier cooling. In our case, the effect of cooling (< 2ps) cannot be observed due to the interference of thermal lensing occurred in that time scale. Assuming that the hot carrier cooling was completed within the picosecond region, the long lifetimes in the grain boundaries indicate that the grain-to-grain interaction is weak and there would be more chance for the cold charge carriers in the surface trap

states to transfer to the charge extraction layers. However, the rate of charge extraction depends on the interfacial properties between perovskite and the charge-extraction layer. Therefore, more characterizations are needed to understand the charge extraction property for trapped charges in GB and free charges in GI in order to enhance the device performance of a PSC.

In conclusion, a direct mapping approach is reported in this work for that the fs TAM image of a polycrystalline perovskite film can be overlapped pixel-by-pixel with the TEM image. This is for the first time the carrier relaxation dynamics can be correlated directly on varied areas of a well-prepared perovskite film showing uniform and close-packed morphology. We fitted the lifetime distributions of the two samples with two Gaussian functions, for which the short and long lifetime distributions might represent the charge recombination processes for free and trapped carriers, respectively. We then analyzed the lifetime distributions in three normalized TA intensity regions for the two samples. We found that the low-intensity pixels mostly located in the grain boundary region with longer mean lifetimes whereas the high-intensity pixels mostly located in the grain interior region with shorter lifetimes. As a result, the small grains with more contributions from the GB feature longer lifetimes than the large grains for the grain size smaller than 500 nm. For the grains larger than 500 nm, the mean lifetimes are independent on the grain size up to 900 nm. Our results thus indicate that the surface trap states in the grain boundaries with retarded charge recombination (longer lifetimes) might play a role for efficient charge extraction to the contact layer. The TAM work on the effect of charge extraction from perovskite to varied underlayers is underway.

ACKNOWLEDGMENTS

We thank Prof. Chao-Yu Chung for his instruction and assistance during early stages of the instrumental setup. Ministry of Science and Technology (MOST) in Taiwan provided financial support of this research (MOST 108-2119-M-009-004). This work was also financially supported by the Center for Emergent Functional Matter Science of National Chiao Tung University from The Featured Areas Research Center Program within the framework of the Higher Education SPROUT Project by the Ministry of Education (MOE) in Taiwan.

Keywords: transient absorption microscopy • organo-inorganic halide perovskites • Lifetime mapping • ultrafast imaging • image processing

REFERENCES

[1] H.-S. Kim, C.-R. Lee, J.-H. Im, K.-B. Lee, T. Moehl, A. Marchioro, S.-J. Moon, R. Humphry-Baker, J.-H. Yum, J. E. Moser, et al., *Sci. Rep.* **2012**, *2*, 591.
[2] M. M. Lee, J. Teuscher, T. Miyasaka, T. N. Murakami, H. J. Snaith, *Science* **2012**, *338*, 643–7.
[3] D. Yang, T. Sano, Y. Yaguchi, H. Sun, H. Sasabe, J. Kido, *Adv. Funct. Mater.* **2019**, *29*, 1807556.
[4] L. Zhao, K. M. Lee, K. Roh, S. U. Z. Khan, B. P. Rand, *Adv. Mater.* **2019**, *31*, 1805836.
[5] A. Mikosch, S. Ciftci, G. Tainter, R. Shivanna, B. Haehnle, F. Deschler, A. J. C. Kuehne, *Chem. Mater.* **2019**, *31*, 2590–2596.
[6] K. Yan, M. Peng, X. Yu, X. Cai, S. Chen, H. Hu, B. Chen, X. Gao, B. Dong, D. Zou, *J. Mater. Chem. C* **2016**, *4*, 1375–1381.
[7] J. M. Ball, A. Petrozza, *Nat. Energy* **2016**, *1*, 16149.
[8] Z. Chu, M. Yang, P. Schulz, D. Wu, X. Ma, E. Seifert, L. Sun, X. Li, K. Zhu, K. Lai, *Nat. Commun.* **2017**, *8*, 2230.
[9] H. Do Kim, H. Ohkita, *Jpn. J. Appl. Phys.* **2018**, *57*, 08RE03.
[10] O. G. Reid, M. Yang, N. Kopidakis, K. Zhu, G. Rumbles, *ACS Energy Lett.* **2016**, *1*, 561–565.
[11] H. Do Kim, H. Ohkita, H. Benten, S. Ito, *Adv. Mater.* **2016**, *28*, 917–922.
[12] Y. Ma, Y. Liu, I. Shin, I.-W. Hwang, Y. K. Jung, J. H. Jeong, S. H. Park, K. H. Kim, *ACS Appl. Mater. Interfaces* **2017**, *9*, 33925–33933.
[13] D.-Y. Son, J.-W. Lee, Y. J. Choi, I.-H. Jang, S. Lee, P. J. Yoo, H. Shin, N. Ahn, M. Choi, D. Kim, et al., *Nat. Energy* **2016**, *1*, 16081.
[14] J. S. Yun, A. Ho-Baillie, S. Huang, S. H. Woo, Y. Heo, J. Seidel, F. Huang, Y.-B. Cheng, M. A. Green, *J. Phys. Chem. Lett.* **2015**, *6*, 875–880.
[15] Z. Chu, M. Yang, P. Schulz, D. Wu, X. Ma, E. Seifert, L. Sun, X. Li, K. Zhu, K. Lai, *Nat. Commun.* **2017**, *8*, 2230.
[16] M. Yang, Y. Zeng, Z. Li, D. H. Kim, C.-S. Jiang, J. van de Lagemaat, K. Zhu, *Phys. Chem. Chem. Phys.* **2017**, *19*, 5043–5050.
[17] Y. Wang, W.-H. Fang, R. Long, O. V. Prezhdo, *J. Phys. Chem. Lett.* **2019**, *10*, 1617–1623.
[18] D. W. deQuilettes, S. M. Vorpahl, S. D. Stranks, H. Nagaoka, G. E. Eperon, M. E. Ziffer, H. J. Snaith, D. S. Ginger, *Science* **2015**, *348*, 683–686.
[19] M. J. Simpson, B. Doughty, B. Yang, K. Xiao, Y.-Z. Ma, *J. Phys. Chem. Lett.* **2015**, *6*, 3041–3047.
[20] M. J. Simpson, B. Doughty, B. Yang, K. Xiao, Y.-Z. Ma, *ACS Photonics* **2016**, *3*, 434–442.
[21] J. M. Snaider, Z. Guo, T. Wang, M. Yang, L. Yuan, K. Zhu, L. Huang, *ACS Energy Lett.* **2018**, *3*, 1402–1408.
[22] S. Nah, B. Spokoyny, C. Stoumpos, C. M. M. Soe, M. Kanatzidis, E. Harel, *Nat. Photonics* **2017**, *11*, 285–288.
[23] S. Nah, B. Spokoyny, X. Jiang, C. Stoumpos, C. M. M. Soe, M. G. Kanatzidis, E. Harel, *Nano Lett.* **2018**, *18*, 827–831.
[24] X. Jiang, J. Hoffman, C. C. Stoumpos, M. G. Kanatzidis, E. Harel, *ACS Energy Lett.* **2019**, *4*, 1741–1747.
[25] D. Benetti, E. Jokar, C.-H. H. Yu, A. Fathi, H. Zhao, A. Vomiero, E. Wei-Guang Diau, F. Rosei, *Nano Energy* **2019**, *62*, 781–790.
[26] J. S. Manser, P. V. Kamat, *Nat. Photonics* **2014**, *8*, 737–743.
[27] M. B. Johnston, L. M. Herz, *Acc. Chem. Res.* **2016**, *49*, 146–154.
[28] D. Zhang, M. N. Slipchenko, D. E. Leaird, A. M. Weiner, J. Cheng, S. M. J. Drive, W. Lafayette, *Opt. Express* **2013**, *21*, 2641–2643.